

Star-forming galaxies dominate the diffuse, isotropic γ -ray background

Matt Roth (✉ matt.roth@anu.edu.au)

The Australian National University <https://orcid.org/0000-0002-4204-5026>

Mark Krumholz

Australian National University

Roland Crocker

Australian National University

Silvia Celli

Dipartimento di Fisica dell'Università La Sapienza di Roma

Physical Sciences - Article

Keywords: star-forming galaxies, isotropic γ -ray background, cosmic ray electrons

Posted Date: November 24th, 2020

DOI: <https://doi.org/10.21203/rs.3.rs-106679/v1>

License:  This work is licensed under a Creative Commons Attribution 4.0 International License.

[Read Full License](#)

Version of Record: A version of this preprint was published at Nature on September 15th, 2021. See the published version at <https://doi.org/10.1038/s41586-021-03802-x>.

1 Star-forming galaxies dominate the diffuse, isotropic

2 γ -ray background

3 Matt A. Roth^{1,*}, Mark R. Krumholz^{1,2}, Roland M. Crocker¹, and Silvia Celli³

4 ¹Research School of Astronomy and Astrophysics, The Australian National University, Canberra, Australia

5 ²ARC Centre of Excellence for All-Sky Astrophysics in Three Dimensions (ASTRO-3D), Canberra, Australia

6 ³Dipartimento di Fisica dell'Università La Sapienza e INFN, P. le Aldo Moro 2, 00185 Rome, Italy

7 *matt.roth@anu.edu.au

8 ABSTRACT

The *Fermi* Gamma Ray Space Telescope has revealed a diffuse, isotropic γ -ray background at energies ranging from 0.1 GeV to 1 TeV [1] whose astrophysical sources remain uncertain. Previous efforts to understand the origin of this background have been hampered by the lack of physical models capable of predicting the γ -ray emission produced by the many candidate sources, which include star-forming galaxies (SFGs) [2–6], active galactic nuclei (particularly blazars [7–9]), millisecond pulsars [7], and dark matter annihilation [10]. In the absence of predictive models, estimates of the contribution from potential sources have relied on a highly-uncertain process of empirically scaling the emission from a small sample of local, resolved sources by their estimated cosmological abundances. Here we present the first calculation of the contribution of SFGs to the γ -ray background that is based on a physical model for the γ -ray emission produced when cosmic ray ions accelerated in supernova remnants interact with the interstellar medium [11]. We validate the model by showing that it reproduces the γ -ray spectra, source count distribution and far infrared- γ -ray correlation observed for nearby, resolved SFGs. When we apply the model to the observed cosmological SFG population, we recover an excellent match to the γ -ray background from 1 GeV to 1 TeV. Our result shows that SFGs alone can explain the full diffuse γ -ray background over this energy range, and strongly suggests that emission in excess of our model at energies < 1 GeV originates from cosmic ray electrons produced in the same galaxies.

10 1 Introduction

The γ -ray sky has been measured exquisitely by the Large Area Telescope (LAT) on board the *Fermi* Gamma Ray Space Telescope over more than a decade. The observed emission can be decomposed into resolved sources – which include pulsar wind nebulae, millisecond pulsars, supernova remnants, and active galactic nuclei (mostly blazars [12]) – and diffuse emission. The diffuse component can be further separated into Galactic foreground emission and an isotropic, extragalactic background [1]. The former is predominantly produced by the interactions of relativistic ions, referred to as cosmic rays (CRs), with the gas that fills the Galaxy between the stars, the interstellar medium (ISM), but the origin of the latter is much more uncertain. SFGs (including the Milky Way) produce diffuse γ -ray emission as a result of diffusive shock acceleration of CRs in

supernova remnants [13]. This process transfers $\sim 10\%$ of the supernova mechanical energy to relativistic particles, yielding on average $\sim 10^{50}$ erg in CR ions per supernova [14, 15], with a substantially smaller portion deposited in CR electrons. The resulting CRs follow a power law distribution in particle momentum, well approximated for relativistic CRs as a power law in total particle energy E [16, 17], $dN/dE \propto E^{-p}$, with an index p that observations of individual supernova remnants, analytical models, and numerical simulations all indicate to be in the range $p \approx 2.0 - 2.6$, with a mean value $p \approx 2.2 - 2.3$ [18, 19]. Some of these CR ions collide inelastically with ISM nuclei, producing roughly equal numbers of π^0 , π^+ and π^- mesons that rapidly decay via the channels $\pi^0 \rightarrow 2\gamma$, $\pi^- \rightarrow \mu^- + \bar{\nu}_\mu$, and $\pi^+ \rightarrow \mu^+ + \nu_\mu$. The decay of π^0 particles is responsible for most of the observed Galactic γ -ray foreground, which displays a characteristic spectrum that rises sharply from $\sim 0.1 - 1$ GeV as a result of the 135 MeV rest mass of the π^0 particle.

2 Galactic emission model

The diffuse γ -ray emission from a SFG depends on three factors: its total star formation rate (which determines its supernova rate and thus the rate at which CRs are injected), the distribution of γ -ray energies produced when individual CRs collide with ISM nuclei (which depends on the parent CR energy E) and the fraction of CRs (again as a function of E) that undergo inelastic collisions before escaping the galaxy. The latter is known as the calorimetry fraction f_{cal} , and is the most poorly-understood of the three.

For the purposes of the calculations we present here, we compute the conversion from star formation rate to CR injection by assuming that stars form with a Chabrier initial mass function [20], which gives the distribution of mass for newly-formed stars, and that stars with initial masses of $8 - 50$ M_\odot , where M_\odot is the mass of the Sun, end their lives as supernovae [21]. Each supernova injects 10^{50} erg of energy in CR ions, distributed in energy for CR energies $E > m_p c^2$ as $d\dot{N}/dE = \phi \dot{M}_* (E/E_0)^{-p} \exp(-E/E_{\text{cut}})$, where $E_0 = 1$ GeV, the cutoff energy $E_{\text{cut}} = 10^8$ GeV¹, \dot{M}_* is the galaxy's star formation rate, and the spectral index $p = 2.2$ [18, 19]. The normalisation factor ϕ that corresponds to our choice of initial mass function, supernova mass range, and CR energy per supernova is $\phi = 6.52 \times 10^{42} \text{ s}^{-1} \text{ GeV}^{-1} M_\odot^{-1} \text{ yr}$.

Similarly, we calculate the γ -ray spectrum produced by CRs of energy E using the parameterised model of Ref. [22], which gives the differential cross section $d\sigma_\gamma/dE_\gamma(E_\gamma, E)$ for the production of γ -rays of energy E_γ by CRs of energy E in inelastic collisions. Combining these factors, the rate at which a SFG produces γ -ray photons is

$$\frac{d\dot{N}_\gamma}{dE_\gamma}(E_\gamma) = \int_{m_p c^2}^{\infty} \frac{d\sigma_\gamma}{dE_\gamma}(E_\gamma, E) \frac{f_{\text{cal}}(E)}{\sigma_{\text{pp}}} \frac{d\dot{N}}{dE}(E) dE \quad (1)$$

where $\sigma_{\text{pp}} = 40$ mbarn is the mean proton-proton inelastic cross-section. The calorimetry fraction $f_{\text{cal}}(E)$ depends on the properties of the galaxy, and the lack of a model for this dependence has previously precluded proper evaluation of Equation 1. However, Ref. [11] recently introduced a model for $f_{\text{cal}}(E)$, based on the idea that the rate at which CRs diffuse through the

¹The exact choice of the cutoff energy above $E \sim \text{PeV}$ makes no practical difference because the injection spectral index $p > 2$, so only a small fraction of the total CR energy is injected at $\gtrsim \text{PeV}$ energies regardless of E_{cut} , and any CRs that are injected at such high energies produce photons that we do not observe due to $\gamma\gamma$ opacity (see below).

43 magnetised ISM, and thus the fraction that escape before colliding, is determined by the balance between driving of turbulence
 44 by the CR streaming instability and ion-neutral damping. This model successfully reproduces the γ -ray spectra of NGC 253,
 45 M82, and Arp 220, and we therefore adopt it for this work. We describe our implementation of the model in detail in the
 46 Methods and illustrate the behaviour of $f_{\text{cal}}(E)$ over a range of gas surface densities and redshifts in Extended Data Figures 1
 47 and 2.

48 The γ -rays produced inside a galaxy do not propagate unhindered, but are subject to losses due to pair production in
 49 collisions with far-infrared (FIR) photons inside the source galaxy and with photons that are part of the extragalactic background
 50 light (EBL) that pervades intergalactic space; the latter is generally the more important effect.

We compute the optical depth $\tau_{\gamma\gamma}$ due to galactic FIR photons using the model of Ref. [23], and the optical depth τ_{EBL} due to the EBL using the model of Ref. [24]. Taking these into account, [Equation 1](#) can be used to compute the specific photon flux dF_γ/dE_γ (i.e., the number of photons per unit area, time and energy) received at the Earth from a galaxy at redshift z as

$$\frac{dF_\gamma}{dE_\gamma}(E_\gamma, z) = \frac{(1+z)^2}{4\pi d_L^2(z)} \frac{dN_\gamma}{dE_\gamma}(E_\gamma(1+z)) e^{-\tau_{\text{EBL}}(E_\gamma, z)} e^{-\tau_{\gamma\gamma}(E_\gamma(1+z))} \quad (2)$$

51 where $d_L(z)$ is the luminosity distance of the source. The radiation that is absorbed by the galactic and extragalactic photon
 52 fields is reprocessed to lower energies in the pair-production cascade. In this process, both the electron and positron, from the
 53 initial high energy pair produced, inverse Compton scatter lower energy photons up to γ -ray energies and these, in turn, produce
 54 further pairs, and so on. The photon spectrum from this cascade can be parameterised according to the method developed in
 55 Ref. [25]. For the purposes of our calculation here, we include the effect of the cascade by adding a component to dF_γ/dE_γ
 56 with a spectral shape as computed by Ref. [25], and with a normalisation such that its energy is equal to the integrated energy
 57 lost to photon-photon scattering. In our model the cascade contributes 5 - 20% of the total emission between 1-100 GeV.

58 3 γ -rays from star-forming galaxies

59 We now have a model that predicts the γ -ray emission of a SFG. The next step in our analysis is to apply this model to a galaxy
 60 survey that samples the SFG population out to the epoch of peak cosmological star formation at $z \sim 2$. For this purpose, we
 61 make use of the Cosmic Assembly Near-infrared Deep Extragalactic Legacy Survey (CANDELS) [26] in the GOODS-S field;
 62 for each CANDELS galaxy we extract the stellar mass M_* , star formation rate \dot{M}_* , and effective radius R_e from the analysis of
 63 Ref. [27]. The full sample contains 34,930 galaxies, but we exclude those whose parameters are uncertain because they contain
 64 bright active galactic nuclei, have unreliable redshifts, or lack a good fit to the surface brightness profile. This leaves a sample
 65 of 22,279 galaxies.

66 Before we can apply our model for $f_{\text{cal}}(E)$ to CANDELS, one further step is required: our model depends on the gas surface
 67 density Σ_g , velocity dispersion σ_g , and gas scale height h_g (see Methods), but CANDELS provides only stellar properties,
 68 and there is no comparably-large deep survey that provides information on the gas properties. For this reason, we infer Σ_g ,
 69 σ_g , and h_g from M_* , \dot{M}_* , and R_e using observed correlations between galaxies' gas and stellar properties. To convert between

70 total masses, surface densities, and volume densities, we assume that the galactic disc has an area of $2\pi R_e^2$ and a thickness
 71 of $2h_g$. We then derive the gas surface density from the stellar and star formation rate surface densities, $\Sigma_* = M_*/2\pi R_e^2$ and
 72 $\dot{\Sigma}_* = \dot{M}_*/2\pi R_e^2$, using the empirical Kennicutt-Schmidt relation obtained by Ref. [28]. Likewise, we derive the gas velocity
 73 dispersion from the star formation rate using the empirical relation obtained by Ref. [29]. Finally, we derive the scale height
 74 assuming the galactic disc is in hydrostatic equilibrium [30]. We provide full details of these procedures in the Methods.

75 To verify that this approach predicts reasonably accurate γ -ray spectra, we apply it to four local, resolved galaxies, chosen
 76 to span a wide range of gas and star formation surface densities: Arp 220, NGC 253, M31, and NGC 4945. The input data we
 77 use for these calculations are summarised in Extended Data Table 1, and we show the results of the computation in Figure 1,
 78 where the solid lines show the spectra derived using only stellar data and, for comparison, the dotted lines show the results we
 79 obtain if we add directly-measured gas properties. We see that the fits are slightly improved if we make direct use of gas data
 80 but, even for the stellar data only, our model reproduces the observed γ -ray spectra to better than a factor of 2 for all galaxies at
 81 energies > 1 GeV, and within a factor of ≈ 1.5 for the two more rapidly star-forming galaxies, which, as we show below, are
 82 more akin to the population that dominates the γ -ray background. We do not expect agreement at energies $\lesssim 1$ GeV because
 83 we have not included the leptonic component of the γ -ray emission, which dominates below the $\sim 0.1 - 1$ GeV cutoff in the
 84 hadronic component set by the π^0 rest mass.

85 Having verified that we can obtain accurate predictions of γ -ray spectra from stellar data alone, we carry out two additional
 86 validation steps. First, we examine the correlation between galaxies' FIR and γ -ray luminosities. We calculate the total γ -ray
 87 luminosity in the band $0.1 - 100$ GeV for each galaxy in our sample by multiplying the integrand in Equation 1 by E_γ and
 88 integrating over the γ -ray spectrum. We also convert the star formation rate to an FIR luminosity in the $8 - 1000$ μm band
 89 using the relation in Ref. [3, 31], corrected to a Chabrier IMF [32]. In Figure 2 we show the resulting distribution of galaxies in
 90 the $L_{\text{FIR}} - L_\gamma$ -plane, along with a power law fit to the data (blue dotted line), $L_\gamma/\text{erg s}^{-1} = 10^{27.69}(L_{\text{FIR}}/L_\odot)^{1.19}$. For comparison,
 91 the solid green line shows a fit to the 14 nearby SFGs detected in γ -rays by *Fermi* LAT [33]. Our model prediction shows
 92 excellent agreement with the observed relation, and we note that both the model and the observed correlation differ noticeably
 93 from the calorimetric limit obtained by simply setting $f_{\text{cal}}(E) = 1$ in Equation 2 (red dashed line in the figure). Thus the
 94 agreement is non-trivial, and suggests that our model is correctly predicting the variation in galaxies' calorimetry fractions as a
 95 function of star formation rate.

96 Our second validation test is to compare our model with counts of *resolved* SFGs observed by *Fermi* LAT. We cannot use
 97 the CANDELS catalogue directly for this purpose, because CANDELS has a narrow field of view that provides very little
 98 sampling of galaxies at $z \lesssim 0.1$, whereas these local sources are the only ones *Fermi* LAT can resolve. Instead, we perform
 99 this test by employing a Monte Carlo scheme to simulate a nearby galaxy population that follows the observed distribution
 100 of star formation rates in the local Universe [34, 35], and where the correlation between galaxy star formation rate and γ -ray
 101 luminosity is the same as what our model predicts for the low redshift ($z < 1.5$) part of the CANDELS sample. Full details of
 102 the Monte Carlo procedure, and the statistical method we use to compute confidence intervals on the observed points, are given

103 in the Supplementary Information. We show the results of this calculation in [Figure 3](#).

104 The figure shows that our Monte Carlo simulations predict SFG source counts consistent with observations, with the
105 exception that we do not predict sources as bright as the Milky Way's two satellite galaxies, the Large and Small Magellanic
106 Clouds. This is not surprising, since these are not part of the field galaxy population we are simulating, and are much closer to
107 the Milky Way than we expect any randomly-chosen field galaxy to be.

108 4 The γ -ray background

Having validated our model, we are now ready to compute the contribution of SFGs to the diffuse, isotropic γ -ray background.
We do this by calculating an observed spectrum for each galaxy in the CANDELS sample using [Equation 2](#), and summing over
all galaxies in bins of redshift:

$$\Phi(E_\gamma) = \frac{d^2F_\gamma}{dE_\gamma d\Omega}(E_\gamma) = \frac{1}{\Omega_S} \sum_{j=1}^{n_{\text{zbin}}} f_{\text{corr},j} \sum_{i=1}^{n_{\text{S},j}} \frac{dF_{\gamma,i}}{dE_\gamma}(E_\gamma, z_j) \quad (3)$$

109 Here $\Omega_S = 173 \text{ arcmin}^2$ is the solid angle surveyed by CANDELS, $n_{\text{S},j}$ the number of surveyed galaxies in the j th redshift bin,
110 and n_{zbin} the number of redshift bins. The factor $f_{\text{corr},j}$ is the ratio of the expected total star formation rate in each redshift bin
111 (based on the measured cosmic star formation history [36]) to the sum of the star formation rates of CANDELS galaxies in that
112 bin; its purpose is to correct for the fact that, due to its limited field of view and various observational biases, the distribution of
113 star formation with respect to redshift in CANDELS does not precisely match the total star formation history of the Universe.
114 We use redshift bins of size $\Delta z = 0.1$, chosen to ensure that the number of sample galaxies in each bin is large enough that the
115 uncertainty in the mean spectrum due to Poisson sampling of the galaxy population is small.

116 We present the results of this calculation in [Figure 4](#). The figure shows that the expected contribution of SFGs to the diffuse
117 isotropic γ -ray background fully reproduces both the intensity and the spectral shape of the observations from $\approx 1 \text{ GeV}$ to ≈ 1
118 TeV. We emphasise that we obtain this agreement from our model with no free parameters: our only inputs are the CR injection
119 spectral index ($p = 2.2$) and the CR energy per supernova (10^{50} erg) that are directly measured in the local Universe, and the
120 distribution of SFGs sampled by CANDELS. The key to the success of the model is the galaxy-by-galaxy calculation of the
121 energy-dependent calorimetry fraction $f_{\text{cal}}(E)$. To illustrate this point, we also show (orange dashed line) the result we would
122 obtain simply by setting $f_{\text{cal}} = 1$ for all galaxies at all energies, which clearly both overestimates the intensity and yields a
123 spectral slope that is flatter than observed. By contrast, the EBL is important for the spectral shape only for energies $> 100 \text{ GeV}$,
124 as illustrated by the green dashed line in [Figure 4](#), which shows the result of a calculation where we omit $\gamma\gamma$ opacity effects.

125 We show the relative contributions to the background made by galaxies with differing star formation rates and redshifts in
126 Extended Data Figure 3. The figure shows that the background at lower energies is dominated by galaxies from just after cosmic
127 noon ($z \sim 1 - 2$), while at higher energies where EBL attenuation has a larger effect, the dominant contribution shifts toward
128 lower redshift, so that at 1 TeV the background is dominated by $z \sim 0.1$ sources. At all energies the dominant contribution
129 comes from galaxies at the upper end of the star-forming main sequence, which have high but not extreme star formation rates

130 for their redshift.

131 5 Discussion

132 It is important to put our finding that SFGs dominate the diffuse, isotropic background in the context of recent work, where a
133 number of authors have argued that blazars and other AGN sources contribute significantly or even dominate the background.
134 We find that, while blazars dominate the *resolved* component of the extragalactic γ -ray background, as shown in [Figure 3](#),
135 SFGs dominate the unresolved component. This finding is consistent with statistical analyses of angular fluctuations in the
136 isotropic background and cross-correlations between it and galaxies and quasars, which strongly disfavour blazars as a dominant
137 contributor [[4](#), [7](#), [37](#)]. Indeed, a straightforward extrapolation of the number counts of observed blazars [[38](#)], illustrated by the
138 orange band in [Figure 3](#), also suggests that blazars do not dominate the unresolved background.

139 Our finding that SFGs alone are able to reproduce the full background also stands in contrast with some earlier analyses
140 (e.g. [[3](#), [39](#)]), though it is consistent with the conclusion of Refs. [[5](#)] and [[40](#)] that, in the absence of either a physical model
141 for the γ -ray emission of SFGs or a much larger sample of resolved galaxies, it is not possible to rule them out as a dominant
142 contributor. It is nonetheless instructive to examine the precise reasons why our conclusions differ from some earlier work.

143 One contributing factor is that earlier models were forced to adopt single power laws for the emitted γ -ray spectrum
144 in different classes of galaxies [[39](#), [41](#)]. By contrast, [Figure 1](#) demonstrates that none of the four nearby resolved galaxies
145 shown have spectra that are well described by a γ -ray spectrum in the form of a pure power law over the energy range from
146 $E_\gamma = 1 - 1000$ GeV; our model correctly captures this behaviour, but earlier pure power law models did not. Similarly, we
147 calculate f_{cal} as a function of energy directly, rather than relying on an empirical FIR- γ correlation, and our calorimetry
148 fractions are on average larger than those implicitly assumed in earlier works. This is because many of the lower estimates
149 for the contribution from SFGs to the γ -ray background rely on a FIR- γ relation derived from early *Fermi* detections of < 10
150 individually-resolved SFGs [[3](#)] that yields somewhat lower γ -ray luminosities than more recent fits using a larger (but still
151 small) sample of SFGs [[33](#)], and with which our model agrees ([Figure 2](#)). Thus the reason we find that SFGs can produce the
152 full background, whereas earlier models could not, is that our model predicts γ -ray emission that is both somewhat brighter and
153 has a more complex spectral shape than the values adopted in earlier work.

154 Likewise, earlier claims that a variety of other source classes dominate the diffuse isotropic background have also relied on
155 extrapolated empirical correlations with large uncertainties. For instance Ref. [[42](#)] estimates the contribution from misaligned
156 active galactic nuclei using a radio- γ relation derived from a sample of 16 resolved objects, coupled with a radio luminosity
157 function extrapolated to redshifts considerably higher than those well-sampled by observations [[43](#)]. By contrast, our assignment
158 of γ -ray luminosities to SFGs is based on a physical model that agrees with local observations, and the CANDELS catalogue
159 from which we draw our distribution of SFG properties has very good completeness over the range of redshift and star formation
160 rate that dominates production of the diffuse γ -ray background (see Extended Data Figure 3).

161 We conclude this discussion with two final questions and one prediction. The first question is whether SFGs can also

162 explain the background below 1 GeV as arising from the leptonic counterpart to the hadronic emission we have measured.
163 Comparing the total power in the γ -ray background from 0.1 – 1 GeV to the total available power in hadronic cosmic rays (the
164 integral under the orange dashed line in [Figure 4](#)) indicates that a small fraction of the hadronic power would be sufficient to
165 explain the observed signal, so this explanation is plausible on energetic grounds. However, we leave detailed modelling of the
166 leptonic emission for future work. The second question is whether SFGs also dominate the observed neutrino background
167 at energies > 1 TeV. We address this issue in the Supplementary Information, where we show that our model implies that
168 SFGs can contribute up to $\approx 15\%$ of the neutrino background at 100 TeV if we set $E_{\text{cut}} = 100$ PeV, but can be much smaller
169 if $E_{\text{cut}} \lesssim 1$ PeV. We show the neutrino spectrum predicted for $E_{\text{cut}} = 1$ and 100 PeV in Extended Data Figure 4, but warn
170 that these results are sensitive to both the statistics of nearby, bright sources that are poorly sampled by CANDELS and the
171 precise shape of the CR spectrum at very high energies. We leave a more thorough exploration of this issue for future work
172 as well. Finally, we note that observations by the upcoming Cherenkov Telescope Array [\[44\]](#) and Large High Altitude Air
173 Shower Observatory [\[45\]](#) should significantly extend the population of γ -ray detected SFGs, in addition to probing the spectra
174 of currently detected SFGs to higher energies. Our model makes clear predictions for both source counts and spectral shapes
175 that can be tested against these data.

176

177 Supplementary Information is available for this paper. Correspondence and requests for materials should be addressed to
178 the first author. Reprints and permissions information is available at www.nature.com/reprints.

179 **Figures**

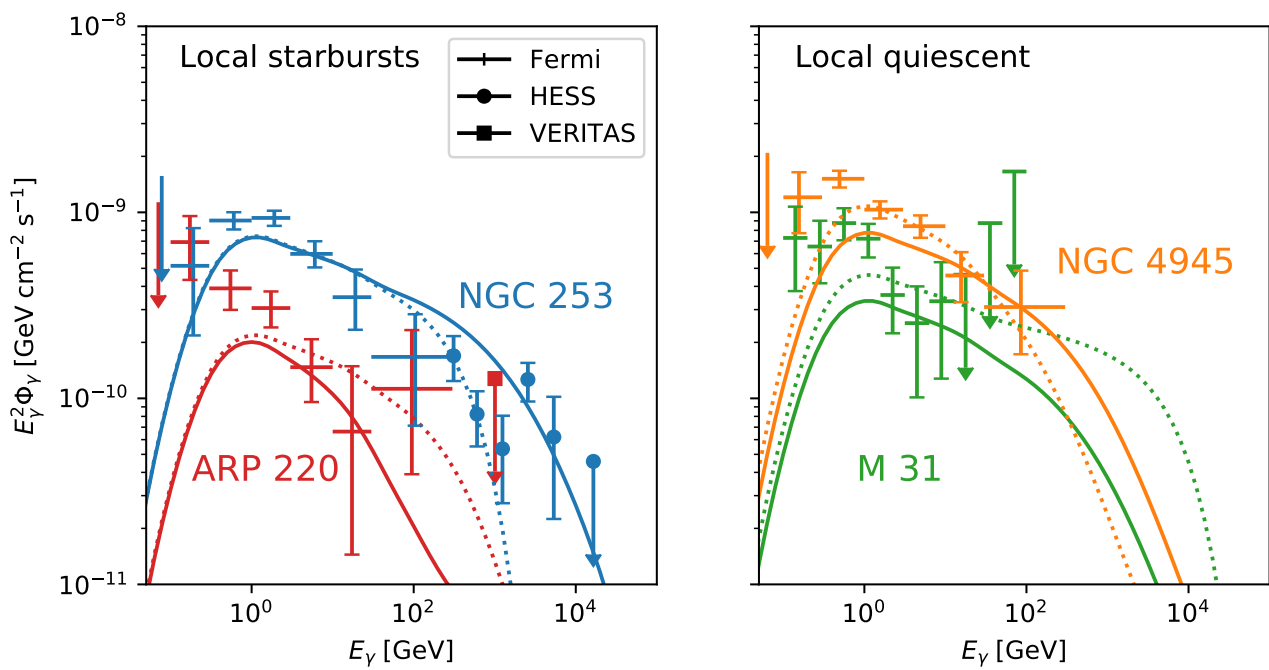


Figure 1. Predicted (lines) and observed (points) γ -ray spectra for a selection of nearby star-forming galaxies detected in γ -rays. The observations shown are taken from a combination of *Fermi* LAT [46], HESS [3], and VERITAS [47]; in the left panel we show the local starburst galaxies Arp 220 and NGC 253, and in the right panel we show the local quiescent galaxies M31 and NGC 4945. The solid lines show model predictions using only stellar data of the type we have available for the CANDELS sample, while the dotted lines shows results predicted if we supplement this with observed gas data. We list the full set of observed quantities used in computing these models in Extended Data Table 1.

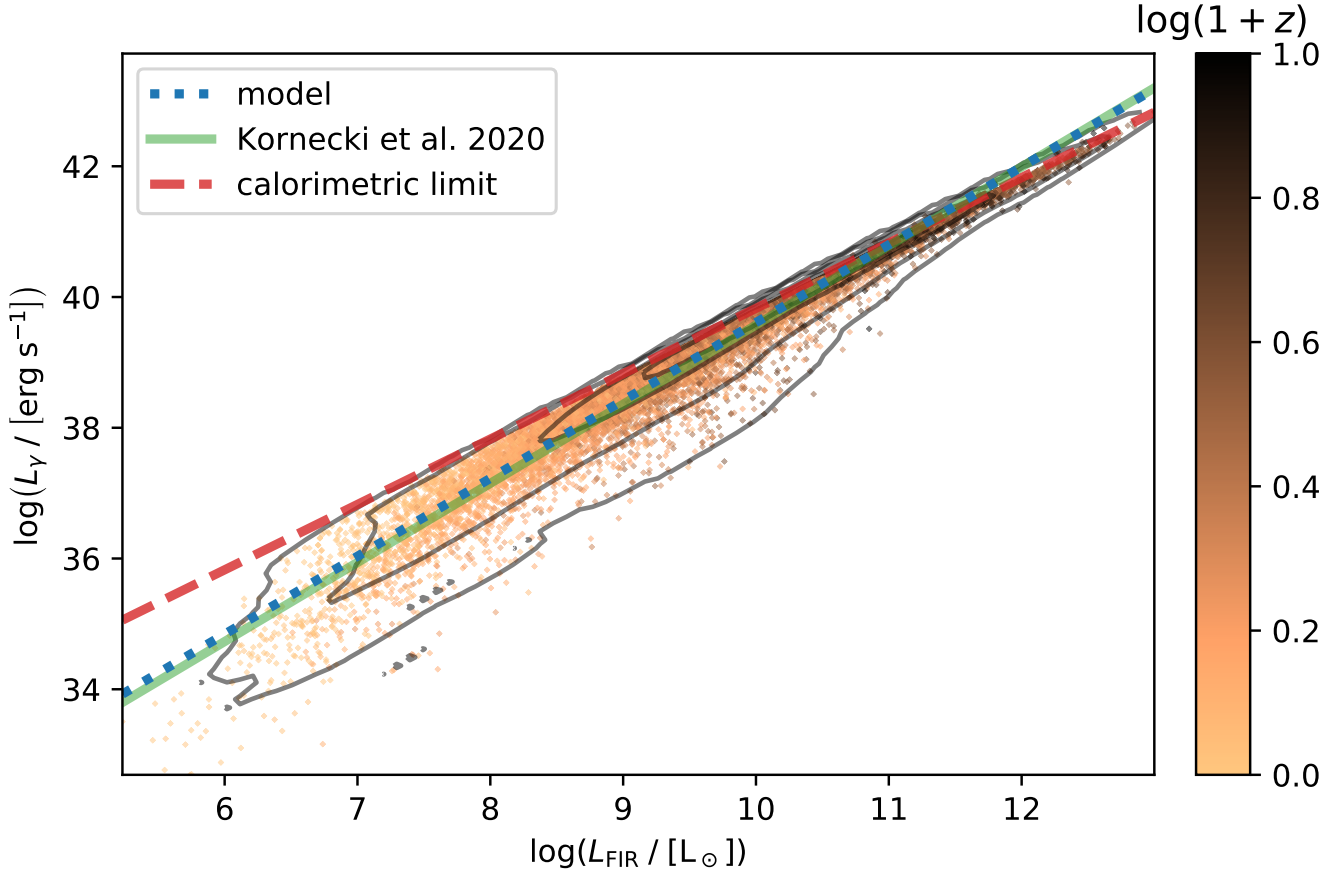


Figure 2. The correlation between far-infrared ($8 - 1000 \mu\text{m}$) and γ -ray ($0.1 - 100 \text{ GeV}$) luminosity for the CANDELS GOODS-S sample, derived using our model. Points show individual CANDELS galaxies, colour-coded by redshift z . Contours show density fractions of 0.002, 0.02, 0.2 and 0.6, computed from a kernel density estimate of the distribution of CANDELS galaxies in the FIR- γ plane. The dashed blue line is a power law fit to the CANDELS sample. For comparison, the solid green line shows the empirical relation measured for 14 nearby, resolved SFGs [38], and the red dashed line is the calorimetric limit obtained by taking $f_{\text{cal}}(E) = 1$ at all energies in Equation 1, as obtained by Ref. [3].

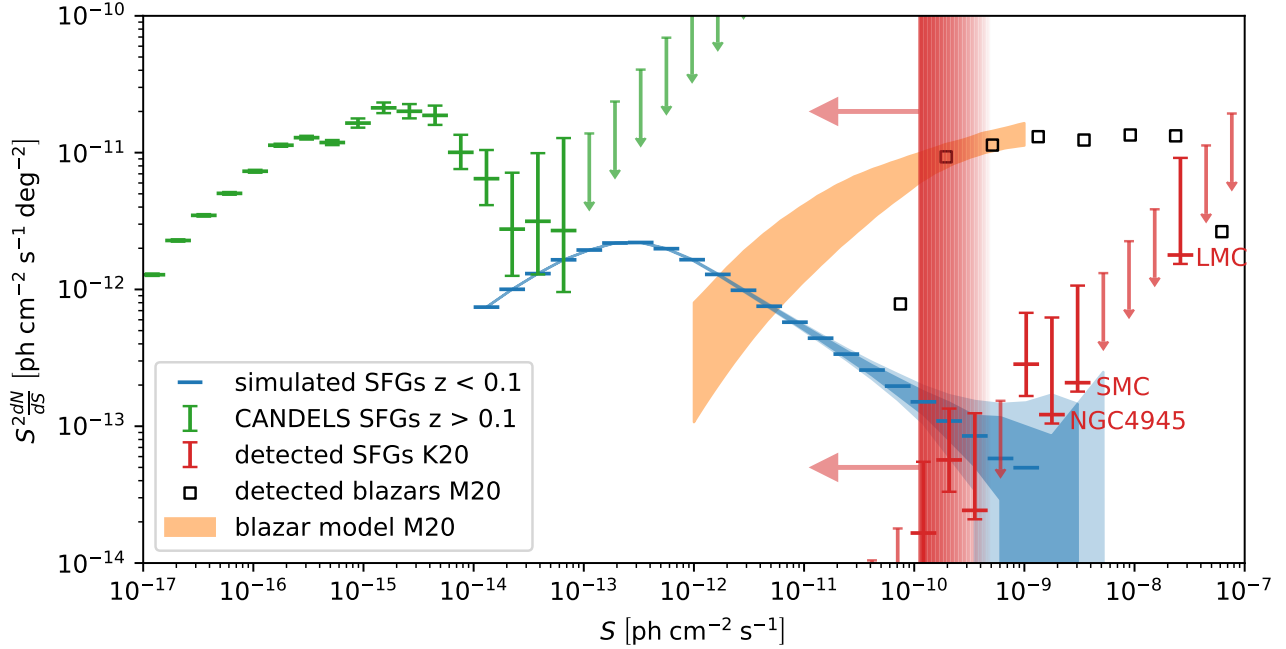


Figure 3. The compensated distribution of γ -ray sources $S^2(dN/dS)$ on the sky as a function of photon flux S integrated from 1 - 100 GeV as seen by *Fermi* LAT. Red and green points show *Fermi*-detected SFGs [33] and model-predicted source counts for observed CANDELS galaxies at $z > 0.1$, respectively; error bars show 90% confidence intervals or upper limits. The three brightest non-empty *Fermi* bins each contain only a single SFG, which we have labelled. Blue points show Monte Carlo realisations of the $z < 0.1$ SFG population, with the light and dark shaded bands indicating 68% and 90% confidence intervals. Black squares show *Fermi*-detected blazars, and the orange band shows the blazar distribution model of Ref. [38]. Finally, the red vertical band indicates the flux range over which *Fermi* observations become incomplete; the left edge of this band is the 4FGL threshold for 98% detection efficiency for sources with spectral index 2.3 [38].

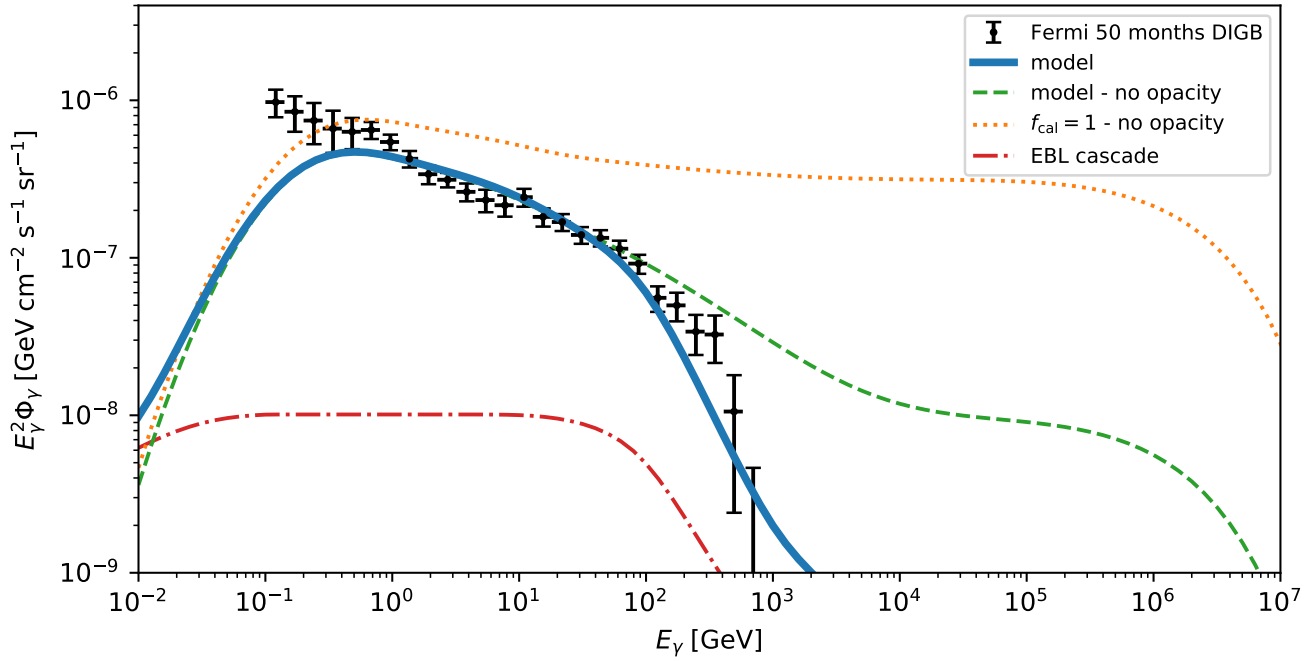


Figure 4. The diffuse isotropic γ -ray background. Black data points show *Fermi* 50-month observations [1]; the blue line shows our prediction for the background due to SFGs; the red dot-dashed line shows the contribution to this spectrum due to the $\gamma\gamma$ scattering cascade, and the green dashed line shows the spectrum we would obtain in the absence of $\gamma\gamma$ opacity. For comparison, the orange line is the model prediction for full calorimetry, i.e., with $f_{\text{cal}}(E) = 1$ for all galaxies at all CR energies.

180 **Acknowledgements**

181 This research has made use of the NASA/IPAC Infrared Science Archive, which is funded by the National Aeronautics and
182 Space Administration and operated by the California Institute of Technology. Funding for this work was provided by the
183 Australian Government through the Australian Research Council, awards FT180100375 (MRK) and DP190101258 (RMC
184 and MRK), and the Australian National University through a research scholarship (MAR). RMC thanks Oscar Macias and
185 Shin'ichiro Ando for enlightening conversations while a Kavli IPMU-funded guest of the GRAPPA Institute at the University
186 of Amsterdam.

187 **Author contributions**

188 All authors were involved in the design of the study and the interpretation of the results. MAR performed the modelling and
189 data analysis with input from MRK, RMC, and SC. The manuscript was written by MAR, MRK and RMC, and reviewed by all
190 authors.

191 **Methods**

192 **Model for calorimetry**

We employ the model of Ref. [11] for CR transport and calorimetry in SFGs. The basic premise of the model is that, in the neutral phase that dominates the mass of the ISM and thus the set of available targets for γ -ray production, CR transport is primarily by streaming along magnetic field lines. However, this yields approximately diffusive transport when averaged over scales comparable to or larger than the coherence length of the magnetic field, with a diffusion coefficient $D \approx V_{\text{st}} h_g / M_A^3$, where V_{st} is the CR streaming speed, h_g is the gas scale height, and M_A is the Alfvén Mach number of the turbulence. For diffusive transport with losses in a disc geometry, the calorimetry fraction is given by (using the favoured parameters of Ref. [11])

$$f_{\text{cal}}(E) = 1 - \left[{}_0F_1 \left(\frac{1}{5}, \frac{16}{25} \tau_{\text{eff}} \right) + \frac{3}{4} \frac{\tau_{\text{eff}}}{M_A^3} {}_0F_1 \left(\frac{9}{5}, \frac{16}{25} \tau_{\text{eff}} \right) \right]^{-1}, \quad (4)$$

where ${}_0F_1$ is the generalised hypergeometric function and τ_{eff} is the dimensionless effective optical depth of the ISM, given by

$$\tau_{\text{eff}} = \frac{\sigma_{\text{pp}} \eta_{\text{pp}} \Sigma_g h_g c}{2 D_0 \mu_p m_H}. \quad (5)$$

193 Here $\sigma_{\text{pp}} = 40$ mbarn is the mean proton-proton inelastic cross section, $\eta_{\text{pp}} = 0.5$ is the elasticity of pp collisions, Σ_g is the gas
194 surface density of the galactic disc, c is the speed of light, D_0 is the diffusion coefficient at the galactic midplane, $\mu_p = 1.17$ is
195 the number density of nucleons per proton, and $m_H = 1.67 \times 10^{-24}$ g is the mass of a hydrogen atom.

To evaluate the calorimetry fraction for a CR of energy E , we must therefore determine the midplane diffusion coefficient D_0 for CRs of that energy, which in turn depends on the streaming speed V_{st} . This speed is dictated by the balance between excitation of the streaming instability and dissipation of the instability by ion-neutral damping, the dominant dissipation mechanism in the weakly-ionised neutral ISM. Balancing these two effects yields a CR proton streaming velocity

$$V_{\text{st}} \approx \min \left[c, V_{\text{Ai}} \left(1 + \frac{\gamma_d \chi M_A c \rho^{3/2}}{4 \pi^{1/2} C e u_{\text{LA}} \mu_i \gamma^{-p+1}} \right) \right] \quad (6)$$

196 where V_{Ai} is the ion Alfvén speed, $\gamma_d = 4.9 \times 10^{13} \text{ cm}^3 \text{ g}^{-1}$ is the ion-neutral drag coefficient, χ is the ionised mass fraction,
197 $\rho = \Sigma_g / 2h_g$ is the midplane mass density of the ISM, C is the midplane number density of CRs, e is the elementary charge,
198 u_{LA} is the velocity dispersion of Alfvén modes in the ISM at the outer scale of the turbulence, μ_i is the atomic mass of the
199 dominant ion species, p is the index of the CR energy distribution, and $\gamma = E/m_p c^2$ is the Lorentz factor of the CR. Since
200 γ -ray production in our model is dominated by galaxies with high star formation rates and gas surface densities within which i)
201 the ISM is molecule-dominated, ii) the main ionised species is C^+ , and iii) the magnetic field is set by a turbulent dynamo,
202 we adopt the fiducial parameters of Ref. [11] appropriate for such galaxies. Specifically, we take $\chi = 10^{-4}$, $\mu_i = 12$, $M_A = 2$,
203 $V_{\text{Ai}} = u_{\text{LA}} / \chi^{1/2} M_A$, and $u_{\text{LA}} = \sigma_g / \sqrt{2}$, where σ_g is the gas velocity dispersion of the galaxy. We also adopt $p = 2.2$, consistent
204 with our assumed injection spectrum.

At this point we have specified all the ingredients required to compute $f_{\text{cal}}(E)$ for a galaxy of known Σ_g , σ_g , and h_g , save one: C , the CR number density. We estimate this as follows: consistent with our discussion in the main text, for a galaxy with star formation rate per unit area $\dot{\Sigma}_*$, the relativistic cosmic ray injection rate per unit area is

$$\frac{d\dot{N}}{dA} = \phi \dot{\Sigma}_* \int_{m_p c^2}^{\infty} (E/E_0)^{-p} e^{-E/E_{\text{cut}}} dE \approx 5.87 \times 10^{42} \dot{\Sigma}_* \text{ s}^{-1} \text{M}_{\odot}^{-1} \text{yr}. \quad (7)$$

The CR number density at the midplane is then given by

$$C \approx \frac{t_{\text{loss}}}{2h_g} \left(\frac{d\dot{N}}{dA} \right), \quad (8)$$

where t_{loss} is the CR loss time. This is given by $t_{\text{loss}} = 1 / (t_{\text{col}}^{-1} + t_{\text{diff}}^{-1})$, where the timescale for losses in inelastic hadronic collisions is $t_{\text{col}} = 1 / (\rho \sigma_{\text{pp}} \eta_{\text{pp}} c / \mu_p m_H)$ and the diffusive escape time $t_{\text{diff}} = 100 h_g^2 D_0^{-1}$, assuming CRs must escape from an extended region of height $\sim 10h_g$. For the systems with high gas densities and high star formation rate that dominate γ -ray production, the loss time is generally dominated by collisional losses. Conversely, for systems forming stars more sedately and with lower density environments, it is generally determined by the diffusive escape time. (Here we have estimated the diffusion coefficient to first order by assuming CRs diffuse close to the ion Alfvén speed.)

Galaxy gas properties

Our calorimetry model requires, as input, the gas surface density Σ_g , scale height h_g , and velocity dispersion σ_g , along with the surface density of star formation $\dot{\Sigma}_*$. However, the CANDELS data set that we use provides only the cosmological redshift z , stellar mass M_* , half-light or effective radius R_e (corrected to 5000 Å according to Ref. [48]), and total star formation rate \dot{M}_* for our sample galaxies. We must therefore estimate the gas properties from observed correlations between gas and stellar properties. We do so as follows.

The half light radius R_e at 5000 Å serves as a first order estimate of how the star formation and matter are distributed throughout the galactic disc. We therefore estimate the star formation rate surface density as $\dot{\Sigma}_* = \dot{M}_*/2\pi R_e^2$ and the stellar surface density as $\Sigma_* = M_*/2\pi R_e^2$. We estimate the gas surface density from the observed correlation between gas, stellar, and star formation surface densities given by Ref. [28]:

$$\frac{\Sigma_g}{\text{M}_{\odot} \text{pc}^{-2}} = 10^{10.28} \frac{\dot{\Sigma}_*}{\text{M}_{\odot} \text{yr}^{-1} \text{pc}^{-2}} \left(\frac{\Sigma_*}{\text{M}_{\odot} \text{pc}^{-2}} \right)^{-0.48} \quad (9)$$

Similarly, there is a strong correlation between galaxy star formation rates and velocity dispersions, which we use to derive σ_g . For this purpose we fit the relationship using the MaNGA galaxy sample [29]. A powerlaw fit to the data obtained in this survey (Fig. 6 of [29]) gives

$$\frac{\sigma_g}{\text{km s}^{-1}} = 32.063 \left(\frac{\dot{M}_*}{\text{M}_{\odot} \text{yr}^{-1}} \right)^{0.096} \quad (10)$$

Finally, we derive the gas scale height under the assumption that the gas is in vertical hydrostatic equilibrium, in which case the scale height is [30]

$$h_g = \frac{\sigma_g^2}{\pi G (\Sigma_g + \Sigma_*)} \quad (11)$$

When applying this model to the galaxies in the CANDELS sample, we take the stellar properties from Ref. [27] and correct the half-light radii to 5000 Å following the procedure outlined in Ref. [48]. This gives us a sufficient set of input parameters to apply our model.

220 **References**

- 221 1. Ackermann, M. *et al.* The Spectrum of Isotropic Diffuse Gamma-Ray Emission between 100 MeV and 820 GeV. **799**, 86.
222 arXiv: [1410.3696 \[astro-ph.HE\]](#) (Jan. 2015).
- 223 2. Fields, B. D., Pavlidou, V. & Prodanović, T. Cosmic Gamma-ray Background from Star-forming Galaxies. **722**, L199–
224 L203. arXiv: [1003.3647 \[astro-ph.CO\]](#) (Oct. 2010).
- 225 3. Ackermann, M. *et al.* GeV Observations of Star-forming Galaxies with the Fermi Large Area Telescope. **755**, 164. arXiv:
226 [1206.1346 \[astro-ph.HE\]](#) (Aug. 2012).
- 227 4. Xia, J.-Q., Cuoco, A., Branchini, E. & Viel, M. Tomography of the Fermi-LAT γ -Ray Diffuse Extragalactic Signal via
228 Cross Correlations with Galaxy Catalogs. **217**, 15. arXiv: [1503.05918 \[astro-ph.CO\]](#) (Mar. 2015).
- 229 5. Linden, T. Star-forming galaxies significantly contribute to the isotropic gamma-ray background. **96**, 083001. arXiv:
230 [1612.03175 \[astro-ph.HE\]](#) (Oct. 2017).
- 231 6. Ajello, M., Di Mauro, M., Paliya, V. S. & Garrappa, S. The γ -Ray Emission of Star-forming Galaxies. **894**, 88. arXiv:
232 [2003.05493 \[astro-ph.GA\]](#) (May 2020).
- 233 7. Cuoco, A., Komatsu, E. & Siegal-Gaskins, J. M. Joint anisotropy and source count constraints on the contribution of
234 blazars to the diffuse gamma-ray background. **86**, 063004. arXiv: [1202.5309 \[astro-ph.CO\]](#) (Sept. 2012).
- 235 8. Di Mauro, M., Calore, F., Donato, F., Ajello, M. & Latronico, L. Diffuse γ -Ray Emission from Misaligned Active Galactic
236 Nuclei. **780**, 161. arXiv: [1304.0908 \[astro-ph.HE\]](#) (Jan. 2014).
- 237 9. Qu, Y., Zeng, H. & Yan, D. Gamma-ray luminosity function of BL Lac objects and contribution to the extragalactic
238 gamma-ray background. **490**, 758–765. arXiv: [1909.07542 \[astro-ph.HE\]](#) (Nov. 2019).
- 239 10. Ajello, M. *et al.* The Origin of the Extragalactic Gamma-Ray Background and Implications for Dark Matter Annihilation.
240 **800**, L27. arXiv: [1501.05301 \[astro-ph.HE\]](#) (Feb. 2015).
- 241 11. Krumholz, M. R. *et al.* Cosmic ray transport in starburst galaxies. **493**, 2817–2833. arXiv: [1911.09774 \[astro-ph.HE\]](#)
242 (Apr. 2020).
- 243 12. Fornasa, M. & Sánchez-Conde, M. A. The nature of the Diffuse Gamma-Ray Background. **598**, 1–58. arXiv: [1502.02866 \[astro-ph.CO\]](#) (Oct. 2015).
- 244 13. Bell, A. R. Cosmic ray acceleration. *Astroparticle Physics* **43**, 56–70 (Mar. 2013).
- 245 14. Woosley, S. E. & Weaver, T. A. *The evolution and explosion of massive Stars II: Explosive hydrodynamics and nucleosynthesis*. NASA STI/Recon Technical Report N. Aug. 1995.
- 246 15. Dermer, C. D. & Powale, G. Gamma rays from cosmic rays in supernova remnants. **553**, A34. arXiv: [1210.8071 \[astro-ph.HE\]](#) (May 2013).

- 250 16. Bell, A. R. The acceleration of cosmic rays in shock fronts - I. **182**, 147–156 (Jan. 1978).
- 251 17. Blandford, R. & Eichler, D. Particle acceleration at astrophysical shocks: A theory of cosmic ray origin. **154**, 1–75 (Oct.
252 1987).
- 253 18. Caprioli, D. Understanding hadronic gamma-ray emission from supernova remnants. **2011**, 026. arXiv: [1103.2624](#)
254 [[astro-ph.HE](#)] (May 2011).
- 255 19. Caprioli, D. Cosmic-ray acceleration in supernova remnants: non-linear theory revised. **2012**, 038. arXiv: [1206.1360](#)
256 [[astro-ph.HE](#)] (July 2012).
- 257 20. Chabrier, G. Galactic Stellar and Substellar Initial Mass Function. **115**, 763–795. arXiv: [astro-ph/0304382](#)
258 [[astro-ph](#)] (July 2003).
- 259 21. Heger, A., Fryer, C. L., Woosley, S. E., Langer, N. & Hartmann, D. H. How Massive Single Stars End Their Life. **591**,
260 288–300. arXiv: [astro-ph/0212469](#) [[astro-ph](#)] (July 2003).
- 261 22. Kafexhiu, E., Aharonian, F., Taylor, A. M. & Vila, G. S. Parametrization of gamma-ray production cross sections for p p
262 interactions in a broad proton energy range from the kinematic threshold to PeV energies. **90**, 123014. arXiv: [1406.7369](#)
263 [[astro-ph.HE](#)] (Dec. 2014).
- 264 23. Razzaque, S., Mészáros, P. & Zhang, B. GeV and Higher Energy Photon Interactions in Gamma-Ray Burst Fireballs and
265 Surroundings. **613**, 1072–1078. arXiv: [astro-ph/0404076](#) [[astro-ph](#)] (Oct. 2004).
- 266 24. Franceschini, A. & Rodighiero, G. The extragalactic background light revisited and the cosmic photon-photon opacity.
267 **603**, A34. arXiv: [1705.10256](#) [[astro-ph.HE](#)] (July 2017).
- 268 25. Berezinsky, V. & Kalashev, O. High-energy electromagnetic cascades in extragalactic space: Physics and features. **94**,
269 023007. arXiv: [1603.03989](#) [[astro-ph.HE](#)] (July 2016).
- 270 26. Grogin, N. A. *et al.* CANDELS: The Cosmic Assembly Near-infrared Deep Extragalactic Legacy Survey. **197**, 35. arXiv:
271 [1105.3753](#) [[astro-ph.CO](#)] (Dec. 2011).
- 272 27. van der Wel, A. *et al.* Structural Parameters of Galaxies in CANDELS. **203**, 24. arXiv: [1211.6954](#) [[astro-ph.CO](#)]
273 (Dec. 2012).
- 274 28. Shi, Y. *et al.* Extended Schmidt Law: Role of Existing Stars in Current Star Formation. **733**, 87. arXiv: [1103.3711](#)
275 [[astro-ph.CO](#)] (June 2011).
- 276 29. Yu, X. *et al.* What drives the velocity dispersion of ionized gas in star-forming galaxies? **486**, 4463–4472. arXiv:
277 [1904.11431](#) [[astro-ph.GA](#)] (July 2019).
- 278 30. Forbes, J., Krumholz, M. & Burkert, A. Evolving Gravitationally Unstable Disks over Cosmic Time: Implications for
279 Thick Disk Formation. **754**, 48. arXiv: [1112.1410](#) [[astro-ph.GA](#)] (July 2012).

- 280 31. Kennicutt Robert C., J. The Global Schmidt Law in Star-forming Galaxies. **498**, 541–552. arXiv: [astro-ph/9712213](#)
281 [[astro-ph](#)] (May 1998).
- 282 32. Crain, R. A., McCarthy, I. G., Frenk, C. S., Theuns, T. & Schaye, J. X-ray coronae in simulations of disc galaxy formation.
283 **407**, 1403–1422. arXiv: [1005.1642](#) [[astro-ph.CO](#)] (Sept. 2010).
- 284 33. Kornecki, P. *et al.* γ -ray/infrared luminosity correlation of star-forming galaxies. **641**, A147. arXiv: [2007.07430](#)
285 [[astro-ph.HE](#)] (Sept. 2020).
- 286 34. Bothwell, M. S. *et al.* The star formation rate distribution function of the local Universe. **415**, 1815–1826. arXiv:
287 [1104.0929](#) [[astro-ph.CO](#)] (Aug. 2011).
- 288 35. Bothwell, M. S. *et al.* Erratum: The star formation rate distribution function of the local Universe. **438**, 3608–3608 (Mar.
289 2014).
- 290 36. Madau, P. & Dickinson, M. Cosmic Star-Formation History. **52**, 415–486. arXiv: [1403.0007](#) [[astro-ph.CO](#)] (Aug.
291 2014).
- 292 37. Ando, S., Fornasa, M., Fornengo, N., Regis, M. & Zechlin, H.-S. Astrophysical interpretation of the anisotropies in the
293 unresolved gamma-ray background. **95**, 123006. arXiv: [1701.06988](#) [[astro-ph.HE](#)] (June 2017).
- 294 38. Manconi, S. *et al.* Testing gamma-ray models of blazars in the extragalactic sky. **101**, 103026. arXiv: [1912.01622](#)
295 [[astro-ph.HE](#)] (May 2020).
- 296 39. Tamborra, I., Ando, S. & Murase, K. Star-forming galaxies as the origin of diffuse high-energy backgrounds: gamma-ray
297 and neutrino connections, and implications for starburst history. **2014**, 043. arXiv: [1404.1189](#) [[astro-ph.HE](#)]
298 (Sept. 2014).
- 299 40. Komis, I., Pavlidou, V. & Zezas, A. Extragalactic gamma-ray background from star-forming galaxies: Will empirical
300 scalings suffice? **483**, 4020–4030. arXiv: [1711.11046](#) [[astro-ph.HE](#)] (Mar. 2019).
- 301 41. Ando, S. & Pavlidou, V. Imprint of galaxy clustering in the cosmic gamma-ray background. **400**, 2122–2127. arXiv:
302 [0908.3890](#) [[astro-ph.HE](#)] (Dec. 2009).
- 303 42. Hooper, D., Linden, T. & Lopez, A. Radio galaxies dominate the high-energy diffuse gamma-ray background. **2016**, 019.
304 arXiv: [1604.08505](#) [[astro-ph.HE](#)] (Aug. 2016).
- 305 43. Willott, C. J., Rawlings, S., Blundell, K. M., Lacy, M. & Eales, S. A. The radio luminosity function from the low-frequency
306 3CRR, 6CE and 7CRS complete samples. **322**, 536–552. arXiv: [astro-ph/0010419](#) [[astro-ph](#)] (Apr. 2001).
- 307 44. Cherenkov Telescope Array Consortium *et al.* *Science with the Cherenkov Telescope Array* (2019).
- 308 45. di Sciascio, G. & Lhaaso Collaboration. The LHAASO experiment: From Gamma-Ray Astronomy to Cosmic Rays.
309 *Nuclear and Particle Physics Proceedings* **279-281**, 166–173. arXiv: [1602.07600](#) [[astro-ph.HE](#)] (Oct. 2016).

- 310 46. Ballet, J., Burnett, T. H., Digel, S. W. & Lott, B. Fermi Large Area Telescope Fourth Source Catalog Data Release 2.
311 *arXiv e-prints*, arXiv:2005.11208. arXiv: [2005.11208 \[astro-ph.HE\]](#) (May 2020).
- 312 47. Peng, F.-K., Wang, X.-Y., Liu, R.-Y., Tang, Q.-W. & Wang, J.-F. First Detection of GeV Emission from an Ultralu-
313 minous Infrared Galaxy: Arp 220 as Seen with the Fermi Large Area Telescope. **821**, L20. arXiv: [1603.06355](#)
314 [[astro-ph.HE](#)] (Apr. 2016).
- 315 48. van der Wel, A. *et al.* 3D-HST+CANDELS: The Evolution of the Galaxy Size-Mass Distribution since $z = 3$. **788**, 28.
316 arXiv: [1404.2844 \[astro-ph.GA\]](#) (June 2014).

Figures

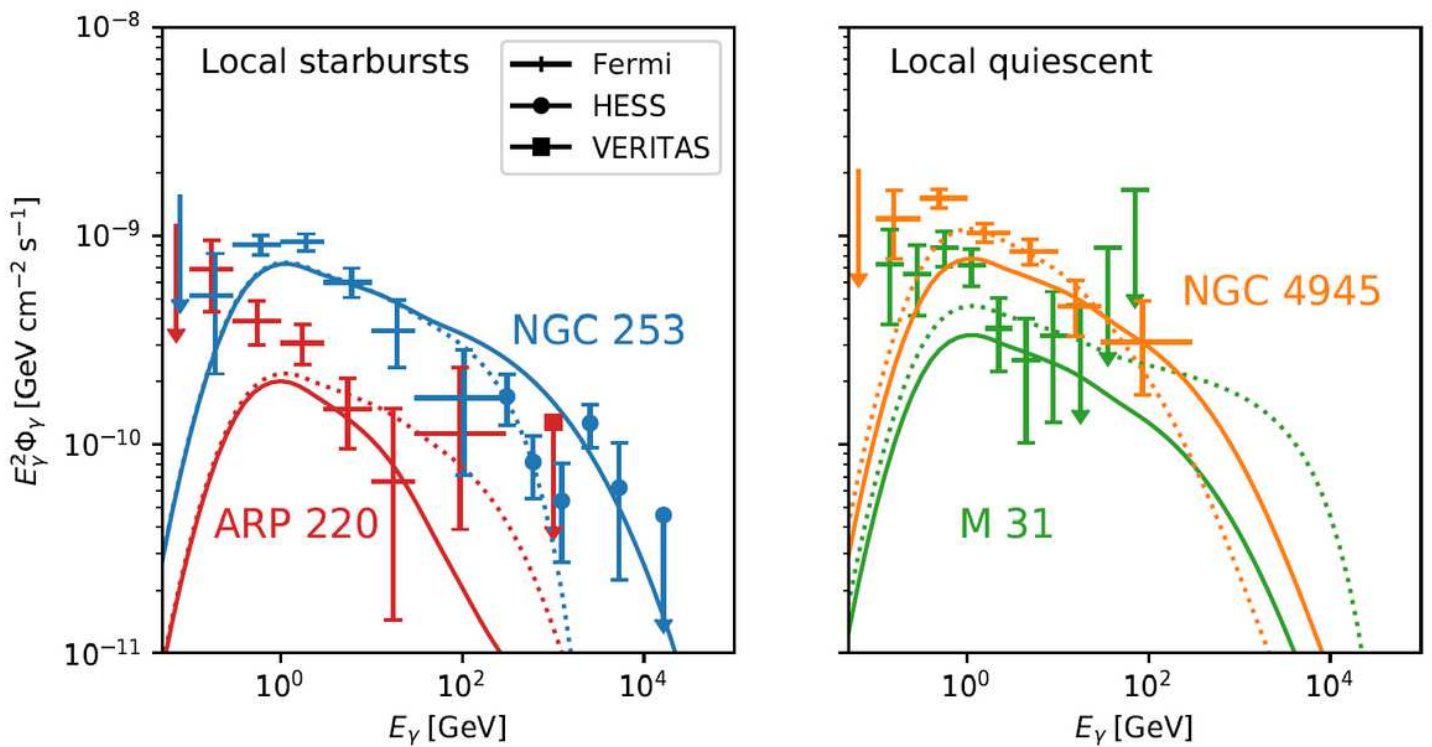


Figure 1

Predicted (lines) and observed (points) γ -ray spectra for a selection of nearby star-forming galaxies detected in γ -rays. The observations shown are taken from a combination of Fermi LAT [46], HESS [3], and VERITAS [47]; in the left panel we show the local starburst galaxies Arp 220 and NGC 253, and in the right panel we show the local quiescent galaxies M31 and NGC 4945. The solid lines show model predictions using only stellar data of the type we have available for the CANDELS sample, while the dotted lines shows results predicted if we supplement this with observed gas data. We list the full set of observed quantities used in computing these models in Extended Data Table 1.

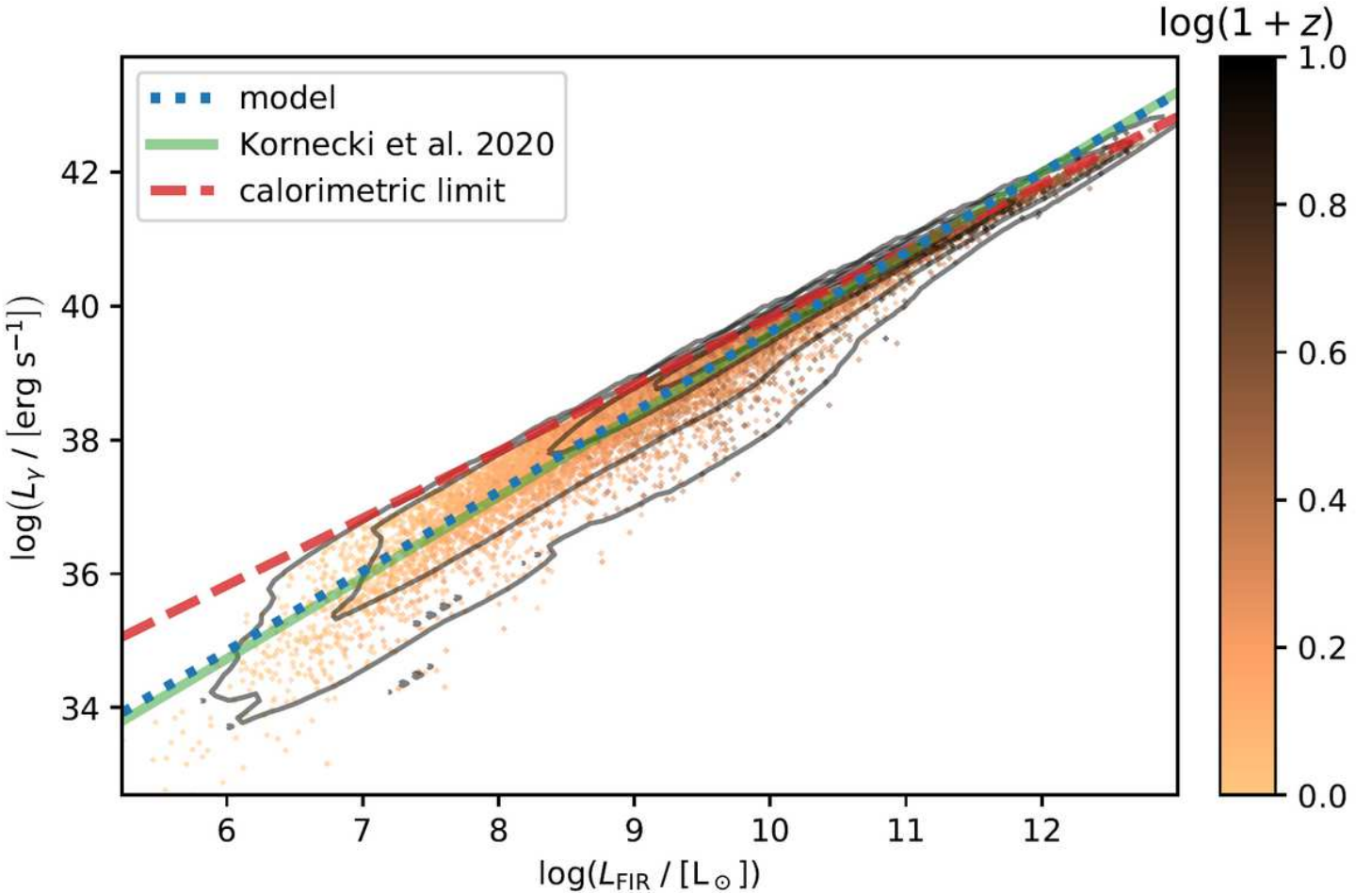


Figure 2

The correlation between far-infrared (8 - 1000 mm) and g-ray (0:1 - 100 GeV) luminosity for the CANDELS GOODS-S sample, derived using our model. Points show individual CANDELS galaxies, colour-coded by redshift z . Contours show density fractions of 0.002, 0.02, 0.2 and 0.6, computed from a kernel density estimate of the distribution of CANDELS galaxies in the FIR- γ plane. The dashed blue line is a power law fit to the CANDELS sample. For comparison, the solid green line shows the empirical relation measured for 14 nearby, resolved SFGs [38], and the red dashed line is the calorimetric limit obtained by taking $f_{\text{cal}}(E) = 1$ at all energies in Equation 1, as obtained by Ref. [3].

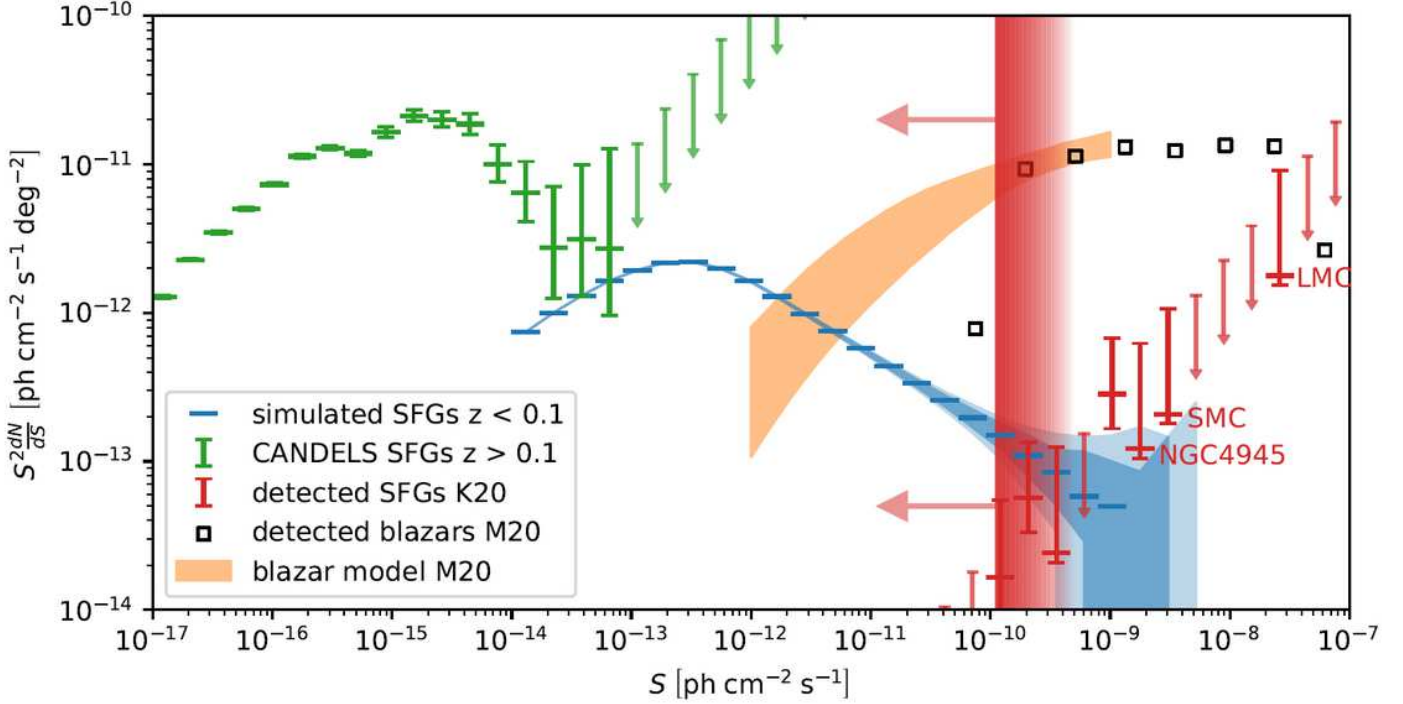


Figure 3

The compensated distribution of γ -ray sources $S^2(dN=dS)$ on the sky as a function of photon flux S integrated from 1 - 100 GeV as seen by Fermi LAT. Red and green points show Fermi-detected SFGs [33] and model-predicted source counts for observed CANDELS galaxies at $z > 0.1$, respectively; error bars show 90% confidence intervals or upper limits. The three brightest non-empty Fermi bins each contain only a single SFG, which we have labelled. Blue points show Monte Carlo realisations of the $z < 0.1$ SFG population, with the light and dark shaded bands indicating 68% and 90% confidence intervals. Black squares show Fermi-detected blazars, and the orange band shows the blazar distribution model of Ref. [38]. Finally, the red vertical band indicates the flux range over which Fermi observations become incomplete; the left edge of this band is the 4FGL threshold for 98% detection efficiency for sources with spectral index 2.3 [38].

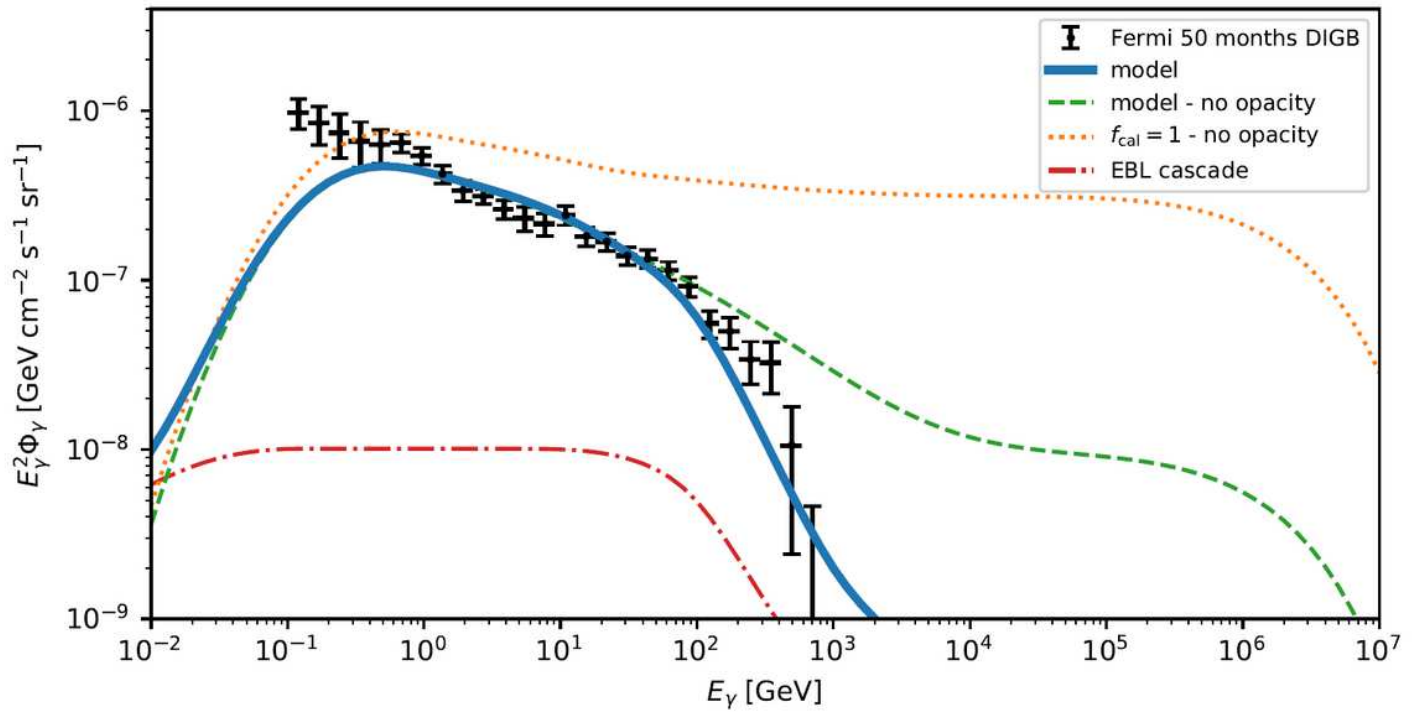


Figure 4

The diffuse isotropic γ -ray background. Black data points show Fermi 50-month observations [1]; the blue line shows our prediction for the background due to SFGs; the red dot-dashed line shows the contribution to this spectrum due to the $\gamma\gamma$ scattering cascade, and the green dashed line shows the spectrum we would obtain in the absence of $\gamma\gamma$ opacity. For comparison, the orange line is the model prediction for full calorimetry, i.e., with $f_{\text{cal}}(E) = 1$ for all galaxies at all CR energies.

Supplementary Files

This is a list of supplementary files associated with this preprint. Click to download.

- [Originofthecosmicgamma raybackgroundSupplementaryInformation.pdf](#)
- [Originofthecosmicgamma raybackgroundExtendedData.pdf](#)